Supplementary Information:
Probing Competing Relaxation Pathways in Malonaldehyde with Transient X-ray Absorption

Nanna H. List,[1,2] Adrian L. Dempwolff,[3] Andreas Dreuw,[3] Patrick Norman[4] and Todd J. Martínez[1,2*]

[1]Department of Chemistry and The PULSE Institute, Stanford University, Stanford, CA 94305

[2]SLAC National Accelerator Laboratory, 2575 Sand Hill Road, Menlo Park, CA 94025

[3]Interdisciplinary Center for Scientific Computing, Heidelberg University, Im Neuenheimer Feld 205, D–69120 Heidelberg, Germany.

[4]School of Engineering Sciences in Chemistry, Biotechnology and Health (CBH), Department of Theoretical Chemistry and Biology, KTH Royal Institute of Technology, Sweden.

[*]toddjmartinez@gmail.com

Contents:

Section S1: Valence-to-core transition properties at the ADC level

In this section, we describe the procedure used for the computation of valence-to-core transition properties using the ADC hierarchy. For completeness, we begin by briefly reviewing the intermediate state representation of ADC.

Originally based on a diagrammatic approach to Green's function theory,[1] the same ADC matrix equations can be derived via the so-called intermediate state representation (ISR).[2, 3] By acting with a general excitation operator, $\hat{C}_J$, on a formally exact electronic ground state, $|\Psi_0\rangle$, "correlated excited states"

$$|\Psi_J^0\rangle = \hat{C}_J |\Psi_0\rangle \tag{1}$$

are formed. The excitation operator consists of creation and annihilation operators $\hat{c}_a^\dagger$ and $\hat{c}_i$ of second quantization,

$$\{\hat{C}_J\} = \{\hat{c}_a^\dagger \hat{c}_i, \hat{c}_b^\dagger \hat{c}_a^\dagger \hat{c}_i \hat{c}_j, \ldots;\ a<b<\ldots, i<j<\ldots\}, \tag{2}$$

where the subscripts $a,b,\ldots$ and $i,j,\ldots$ label virtual and occupied Hartree-Fock (HF) orbitals, respectively. The capital index J thereby denotes general excitations belonging to classes of singles, doubles, etc.

By subsequent orthogonalization of the correlated excited states of each excitation class with respect to the ground state and lower excitation classes, followed by symmetric orthogonalization within the class, a basis of so-called intermediate states (ISs), $\{|\tilde{\Psi}_J\rangle\}$, is constructed. Representing the Hamiltonian, shifted by the electronic ground state energy E_0, within the IS basis, $M_{IJ} = \langle \tilde{\Psi}_I | \hat{H} - E_0 | \tilde{\Psi}_J \rangle$, leads to a Hermitian eigenvalue problem of the form

$$\mathrm{MY} = \mathrm{Y}\boldsymbol{\Omega}, \quad \mathrm{Y}^\dagger \mathrm{Y} = 1. \tag{3}$$

Therein, $\boldsymbol{\Omega}$ is the diagonal matrix of eigenvalues of M, $\Omega_n = E_n - E_0$, being the electronic excitation energies, and Y is the matrix of the corresponding eigenvectors Y_n giving access to the explicit form of excited state wave functions $|\Psi_n\rangle$ via expansion into the IS basis,

$$|\Psi_n\rangle = \sum_J Y_{n,J} |\tilde{\Psi}_J\rangle. \tag{4}$$

Similarly, one-particle operators $\hat{D}$ may be represented within the IS basis as,

$$\tilde{D}_{IJ} = \left\langle \tilde{\Psi}_I \middle| \hat{D} \middle| \tilde{\Psi}_J \right\rangle = \sum_{r,s} d_{rs} \left\langle \tilde{\Psi}_I \middle| \hat{c}_r^\dagger \hat{c}_s \middle| \tilde{\Psi}_J \right\rangle = \sum_{r,s} d_{rs} \tilde{\rho}_{rs}^{IJ}, \tag{5}$$

where $\tilde{\rho}$ is the ISR of the one-particle density, and d_{rs} are matrix elements of $\hat{D}$ in the basis of HF orbitals.[4] Since neither the exact ground state $\left|\Psi_0\right\rangle$ nor its energy E_0 are known they are expanded in a Møller-Plesset (MP) perturbation series, and consequently also the ADC matrix and IS one-particle density are expanded,

$$\mathrm{M} = \mathrm{M}^{(0)} + \mathrm{M}^{(1)} + \mathrm{M}^{(2)} + \ldots \tag{6}$$

$$\tilde{\rho} = \tilde{\rho}^{(0)} + \tilde{\rho}^{(1)} + \tilde{\rho}^{(2)} + \ldots, \tag{7}$$

leading to a hierarchy of ADC(*n*,*m*) methods, where *n* and *m* refer to the order to which M and $\tilde{\rho}$ are expanded, respectively.

We use the core-valence separation (CVS) approximation[5-7] for the description of the core-excited states. In this approximation, the dimensionality of the ADC eigenvalue problem is reduced to the subspace of IS corresponding to singly core-excited configurations, resulting in a lower dimensionality of the CVS-ADC state vectors compared to the full ADC eigenvalue problem.[8, 9] Transition energies between valence- and core-excited states are computed as the difference between the respective excitation energies obtained in the corresponding ADC calculations. For the calculation of transition properties, we exploit the ISR, employing a second-order one-particle transition density matrix-driven approach as implied by Eq. (5). The transition matrix element between two states $|\Psi_n\rangle$ and $|\Psi_m\rangle$

$$\mu_{\alpha,nm} = \left\langle \Psi_n \middle| \hat{\mu}_\alpha \middle| \Psi_m \right\rangle = \sum_{rs} \mu_{\alpha,rs} \sum_{rs} Y_{n,I}^* \tilde{\rho}_{rs,IJ} Y_{m,J}, \tag{8}$$

where $\mu_{\alpha,rs}$ is the representation of the respective component of the dipole operator within the HF orbital basis. Due to the different dimensionality of the involved state vectors, transition dipole moments between valence- and core-excited states were computed after padding the CVS-ADC vectors with zeros to the dimension of the full ADC eigenvalue problem. In particular, no further postprocessing was applied to the core-excited state vectors, implying the computation of transition properties using state vectors not fully converged with respect to the full ADC Hamiltonian. The physical soundness of this approach is in principle not guaranteed since the initial and final states interact (non-orthogonal state vectors), but, as is shown in Section S2, this proves a minor concern in practical cases where CVS is known to be a good approximation.

In principle, there is no general prescription for the choice of the employed ADC schemes. It is rather guided by the expected accuracy in each individual computational step. It should be noted that using the presented methodology, the results obtained for a particular property are only correct up to the lowest order of an individual method involved in its computation. However, the general ADC properties such as size-consistency are inherent to the ISR approach,[10] and no special care needs to be taken in this respect.

Section S2: Validation of approximate ADC valence-to-core transition moments

To evaluate the methodology outlined above for the calculation of transition dipole moments between valence- and core-excited states, we consider the oxygen *K*-edge X-ray absorption of water. The valence- and core-excited states involving this set of orbitals was recently studied with the hierarchy of ADC methods as to determine the resonant inelastic X-ray scattering spectrum of water.[11] Using the 6-311++G** basis set, it was demonstrated that the two lowest core-excited states, mainly described by electronic transitions to LUMO and LUMO+1, respectively, are well described at the ADC(2)-x level of theory. With the aim of validating our procedure, we adopted the small 6-31+G* basis set which allows us to perform a full diagonalization of the complete ADC matrix and determine the errors introduced by use of the CVS approximation to describe the final state in the excitation process.

Figure S1 displays the ground-state X-ray absorption spectrum for water with solid and dashed black lines corresponding to the CVS and full representation of the core-excited states, respectively. The errors in absolute energies associated with the CVS approximation are blue-shifting 0.2–0.4 eV, in line with previous comparisons to the full-space complex polarization propagator approach.[11] Turning to the valence-to-core spectrum with the lowest valence-excited state ($^1B_1$, mainly a single excitation from the $1b_1$ to the $4a_1$ orbital) as reference, the lowest core excitation is $1a_1 \rightarrow 1b_1$, arriving at the $4a_1$ core-excited state. The transition from the valence-excited state to the $2b_2$ core-excited state is symmetry-forbidden and therefore dark in our electric-dipole based spectra. The quality of the CVS-based spectrum for the valence-excited state is comparable to the ground-state spectrum. The non-orthogonality between the valence- and core-excited states is small with a maximum overlap norm below 10^{-4}. The favorable comparison

between the CVS-based procedure for valence-to-core transitions and full diagonalization supports the validity of our approach to simulate NEXAFS spectra from valence-excited states.

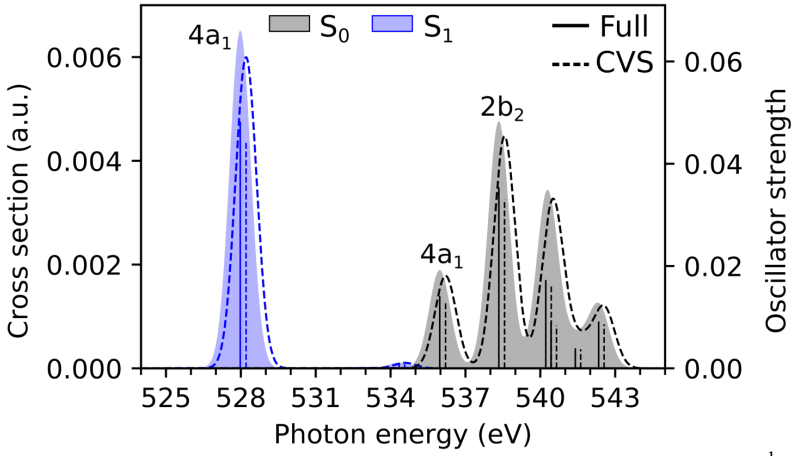

Figure S1 Simulated oxygen *K*-edge X-ray absorption spectra from the ground S_0 ($^1A_1$, black) and valence excited S_1 ($^1B_1$, blue) states of water computed using ADC(2) for the valence-excited state combined with the CVS-ADC(2)-x approximation (dashed) or full diagonalization of the complete ADC(2)-x eigenvalue problem (solid and filled) for the computation of core-excited states. The labels correspond to the valence orbital that is partially occupied in the final core-excited state. Results were obtained with use of the 6-31+G* basis set, and stick spectra were convolved with a Gaussian line shape (FWHM: 1.0 eV).

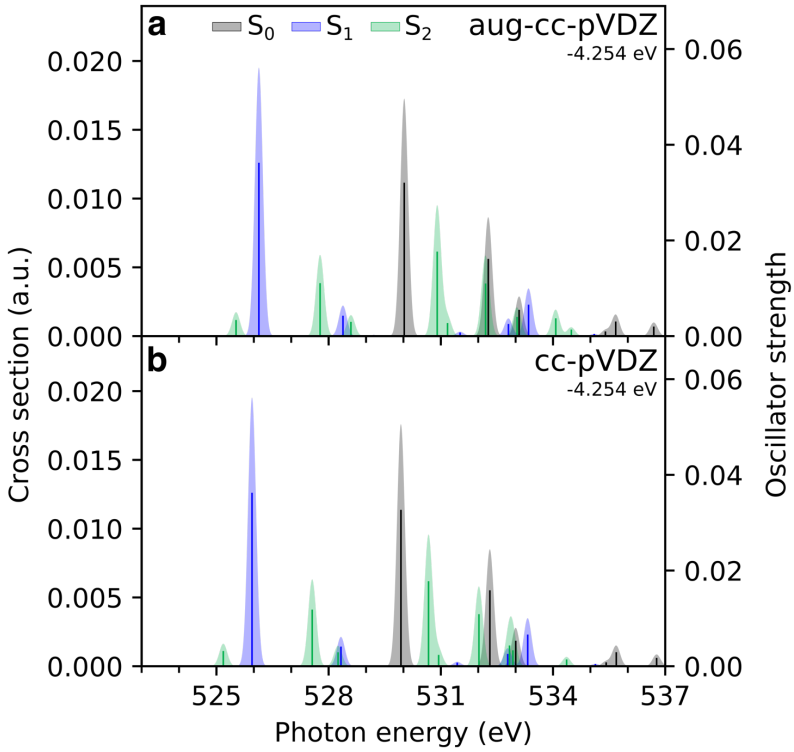

Figure S2 Effect of diffuse functions on the oxygen *K*-edge NEXAFS spectra for the lowest singlet valence states (S_0: black, S_1: blue, S_2: green) at the FC point, computed at the RASPT2(18,0/1,0;2,12,0) level. (a) aug-cc-pVDZ, and (b) cc-pVDZ. Both spectra have been uniformly shifted by -4.254 eV to align the latter with the steady-state spectrum at the ADC level. Stick spectra were convolved with a Gaussian line shape (FWHM: 0.25 eV).

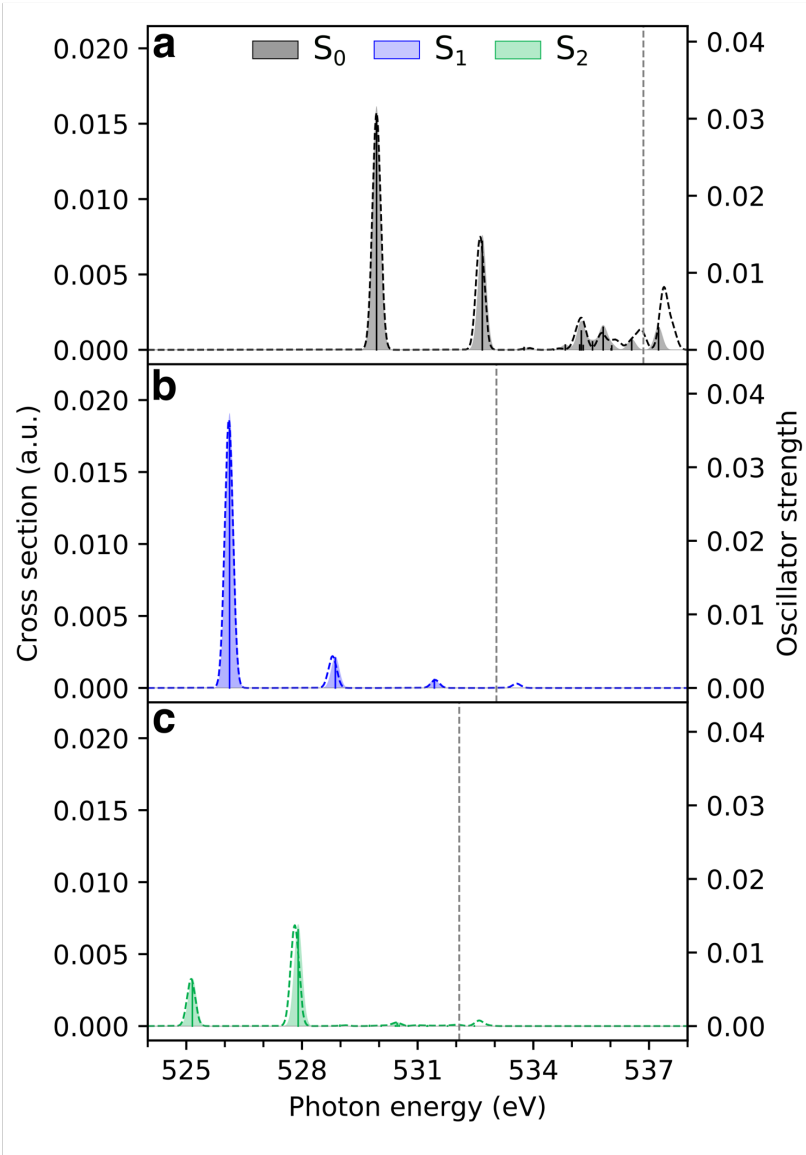

Figure S3 Oxygen *K*-edge NEXAFS spectra from the (a-c) S_0, S_1 and S_2 states of malonaldehyde as obtained with ADC(2)(valence)/CVS-ADC(2)-x(core) using the 6-311++G** (filled) and the 6-31+G* (dashed line) basis sets at the FC point. A shift of -2.625 eV was used to align the 6-31+G* to the 6-311++G** results. Vertical dashed lines indicate the lowest core-ionization potential. Stick spectra were convolved with a Gaussian line shape (FWHM: 0.25 eV).

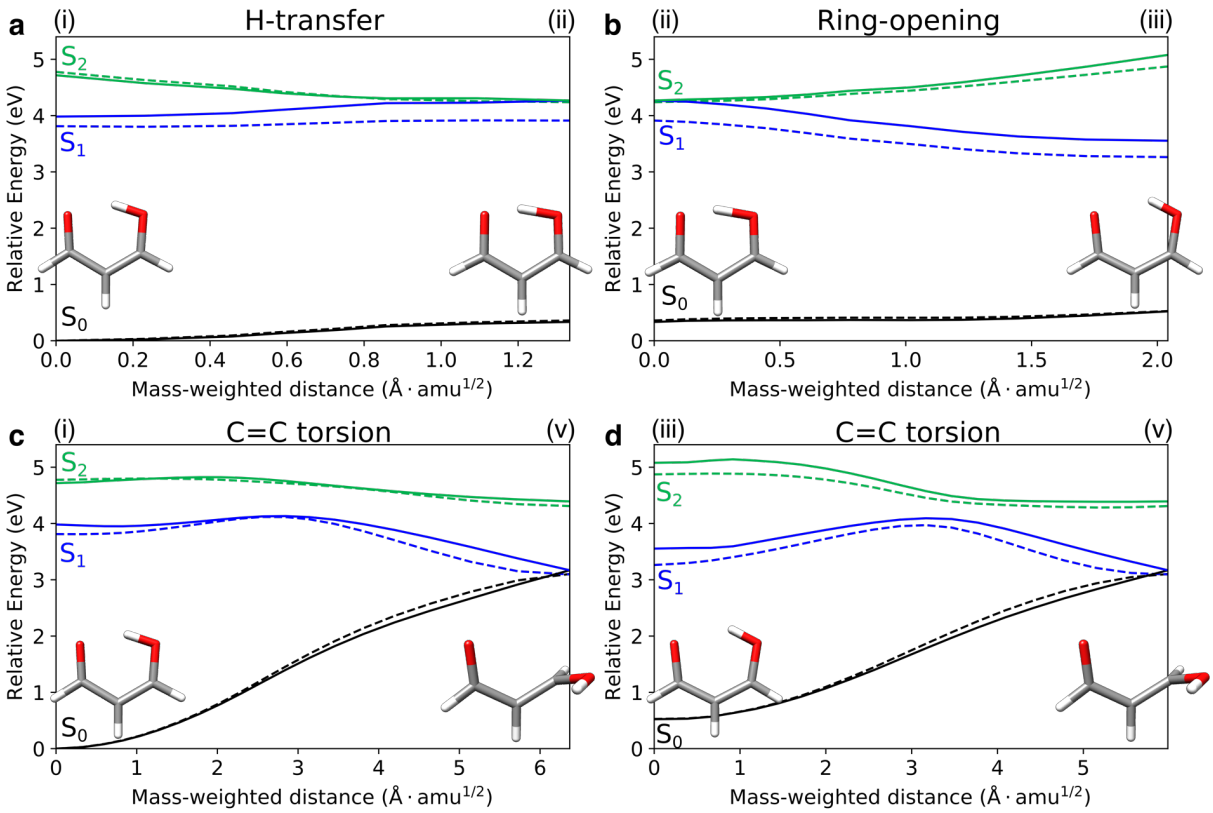

Figure S4 Comparison of potential energy surfaces along geodesic interpolation paths connecting important critical points: (a) H-transfer coordinate $(\mathrm{i}) \rightarrow (\mathrm{ii})$; (b) Ring-opening, $(\mathrm{ii}) \rightarrow (\mathrm{iii})$; (c,d) C=C torsion, $(\mathrm{i}) \rightarrow (\mathrm{v})$ and $(\mathrm{iii}) \rightarrow (\mathrm{v})$ (for labeling, see Figure S7), computed at the ADC(2)/6-311++G** (dashed) and the SA3-XMS-CASPT2(14,12)/cc-pVDZ (solid) level of theory.

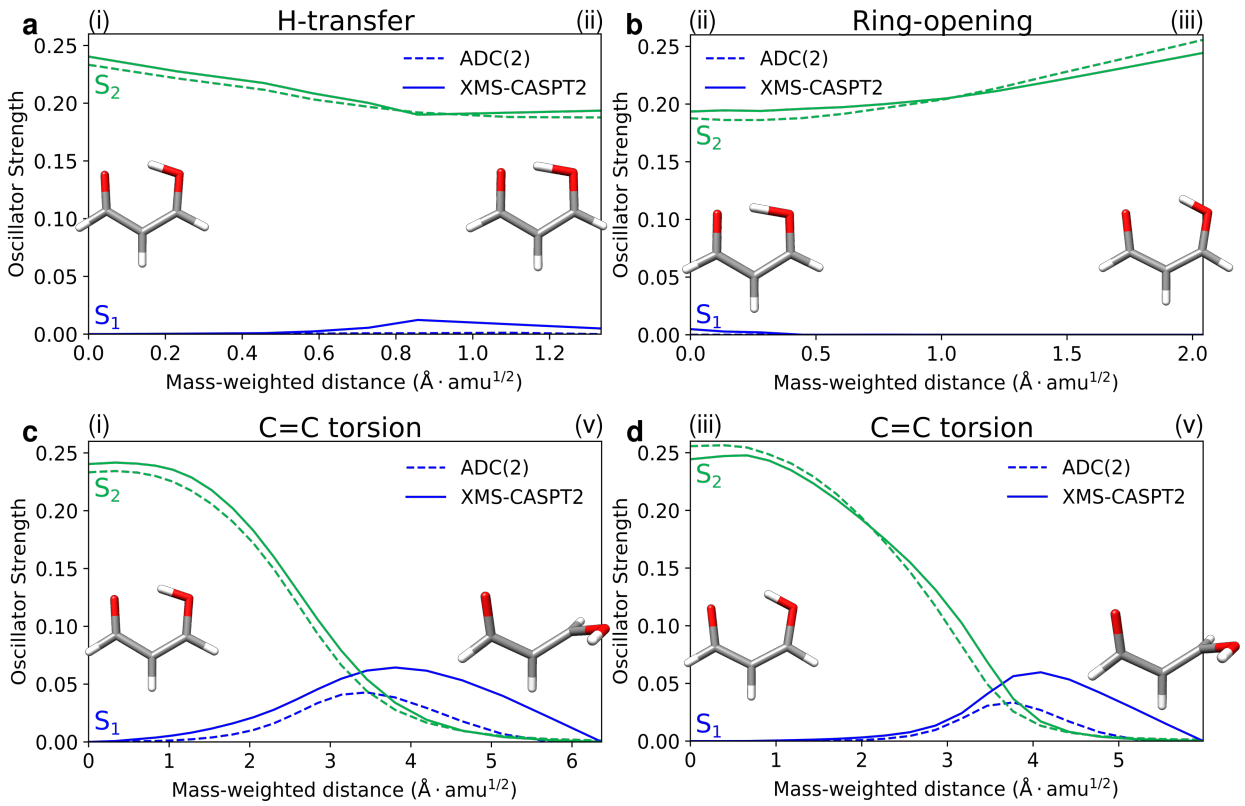

Figure S5 Comparison of oscillator strengths along geodesic interpolation paths connecting important critical points: (a) H-transfer coordinate $(\mathrm{i}) \rightarrow (\mathrm{ii})$; (b) Ring-opening, $(\mathrm{ii}) \rightarrow (\mathrm{iii})$; (c,d) C=C torsion, $(\mathrm{i}) \rightarrow (\mathrm{v})$ and $(\mathrm{iii}) \rightarrow (\mathrm{v})$ (for labeling, see Figure S7), computed at the ADC(2)/6-311++G** (dashed) and the SA3-XMS-CASPT2(14,12)/cc-pVDZ (solid) level of theory. To avoid ambiguity due to arbitrary wavefunction mixing at geometry (ii), the oscillator strengths were computed by linear interpolation between the previous point on the path and an extrapolated point obtained by displacing along the projection of the previous displacement vector onto the branching plane. Note that the results labeled as "XMS-CASPT2" are approximate, based only on the zeroth-order XMS basis.

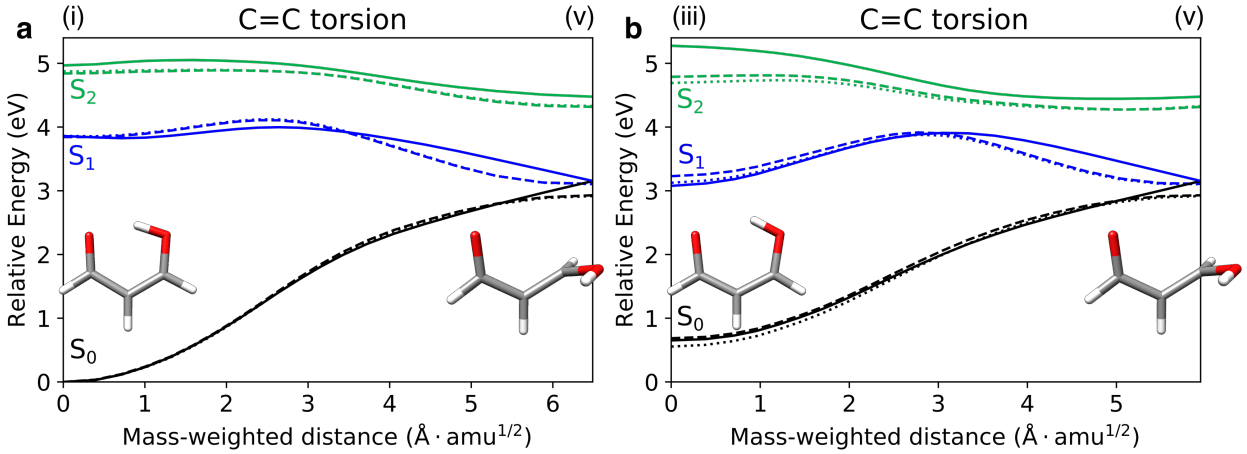

Figure S6 Comparison of potential energy surfaces along geodesic interpolation paths connecting important critical points: (a) C=C torsion $(\mathrm{i}) \rightarrow (\mathrm{v})$ and (b) C=C torsion $(\mathrm{iii}) \rightarrow (\mathrm{v})$, computed at the ADC(2)/6-311++G** (dashed) and the SA4-XMS-CASPT2(4,5)/6-31G* (solid) level of theory. Critical points were obtained at the SA4-XMS-CASPT2(4,5)/6-31G* level of theory except for the FC point that was computed at the MP2 level.

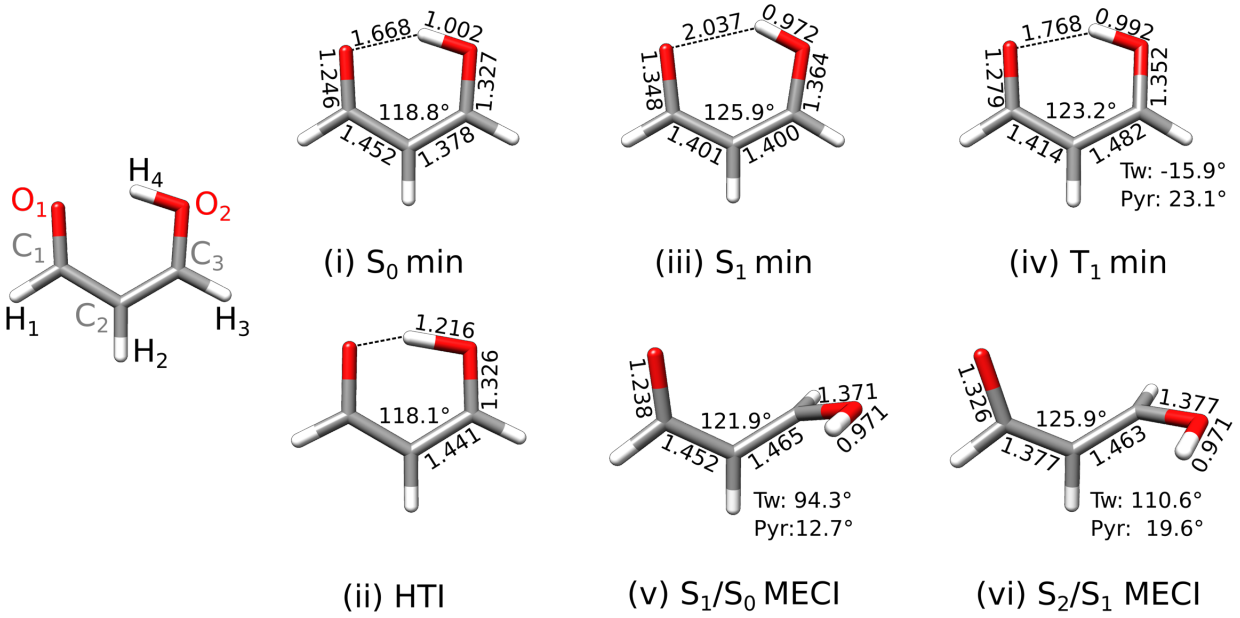

Figure S7 Geometric parameters for critical points obtained at the SA3-XMS-CASPT2(14,12)/cc-pVDZ level of theory. Distances are given in Ångstrom. Tw: $\angle C_1C_2C_3O_2$ dihedral angle, and Pyr: pyramidalization angle of C_3, defined as $\mathrm{pyr}=\cos^{-1}\left\{(R_{C_3O_2}\times R_{C_2H_3})\cdot(R_{C_3H_3}\times R_{C_3C_2})\right\}$.

Table S1 SA3-XMS-CASPT2(14,12)/cc-pVDZ energies (eV) for critical points optimized at the XMS-CASPT2 level. Energies are reported relative to the ground state energy at the FC point.

State\geometry	FC	S_1 min	T_1 min	HTI	S_1/S_0 MECI	S_2/S_1 MECI	S_0 TS(HT)
S_0	0.000	0.522	0.533	0.335	3.169	3.002	0.164
S_1	3.983	3.554	3.915	4.268	3.169	4.046	4.391
S_2	4.717	5.078	4.598	4.268	4.392	4.046	4.453
T_1	3.499	3.428	3.185	3.377	3.277	3.599	3.526
T_2	3.777	3.445	3.815	4.074	4.478	4.137	4.169

Table S2 ADC(2)/6-311++G** energies (eV) for critical points optimized at the SA3-XMS-CASPT2(14,12)/cc-pVDZ level. Energies are reported relative to the ground state energy at the FC point.

State\geometry	FC	S_1 min	T_1 min	HTI	S_1/S_0 MECI	S_2/S_1 MECI	S_0 TS(HT)
S_0	0.000	0.527	0.581	0.360	3.102	3.170	0.141
S_1	3.812	3.262	3.751	3.912	3.095	3.589	4.038
S_2	4.776	4.873	4.560	4.238	4.309	3.701	4.443
T_1	3.505	3.044	3.146	3.453	3.101	3.388	3.587
T_2	3.548	3.385	3.554	3.746	4.289	3.679	3.852

Table S3 Mulliken population analysis of the number of unpaired electron density (using the unpaired electron distribution function in Eq. 18 of Ref. [12]) at the SA3-XMS-CASPT2(14,12)/cc-pVDZ level (based on the zeroth-order XMS basis) at the T_1 minimum, as obtained in this study and as reported by Sapunar *et al.*[13]

Atom	This work	Sapunar *et al.*
O1	0.40	0.24
O2	0.19	0.16
C1	0.12	0.10
C2	0.58	0.69
C3	0.76	0.80

Table S4 Excitation energies (ΔE, eV), oscillator strengths (f), and natural transition and difference density matrix analyses[14] of the two lowest singlet valence excitations, and the five lowest oxygen K-edge transitions from the ground state and valence-excited states. Results were computed using RASPT2(18,0/1,0;2,12,0)/cc-pVDZ. The valence-to-core transition energies have been shifted by -4.254 eV.

Transition	ΔE	f	Ω	n_{ue}	p_{AD}	PR_D	PR_A
S_0-S_1	3.98	0.000	0.82	2.05	1.35	1.78	1.55
S_0-S_2	4.75	0.240	0.85	2.02	1.19	1.46	1.50
S_0-$c_1(O_1)$	529.93	0.032	0.61		2.61	4.88	3.83
S_1-$c_1(O_1)$	525.95	0.043	0.42	2.05	2.23	4.10	3.96
S_2-$c_1(O_1)$	525.18	0.003	0.29		2.74	5.18	4.86
S_0-$c_1(O_2)$	532.31	0.016	0.62		2.66	4.74	4.46
S_1-$c_1(O_2)$	528.33	0.005	0.21	2.05	2.95	5.17	4.92
S_2-$c_1(O_2)$	527.56	0.012	0.28		2.61	4.85	4.13
S_0-$c_2(O_1)$	533.00	0.005	0.19		3.03	5.28	4.22
S_1-$c_2(O_1)$	529.02	0.000	0.00	3.25	2.65	4.55	4.87
S_2-$c_2(O_1)$	528.25	0.003	0.19		2.56	4.71	5.92
S_0-$c_3(O_1)$	535.42	0.001	0.15		3.02	5.30	3.99
S_1-$c_3(O_1)$	531.44	0.001	0.01	3.22	2.68	4.64	4.67
S_2-$c_3(O_1)$	530.67	0.017	0.34		2.52	4.61	4.58
S_0-$c_2(O_2)$	535.69	0.003	0.27		3.06	5.38	5.11
S_1-$c_2(O_2)$	531.71	0.000	0.00	3.28	3.04	5.40	4.93
S_2-$c_2(O_2)$	530.94	0.002	0.12		2.56	4.66	5.20

Ω: Sum of NTO weights, n_{ue}: number of unpaired electrons, p_{AD}: promotion number, $PR_{A/D}$: attachment/detachment partition ratio.

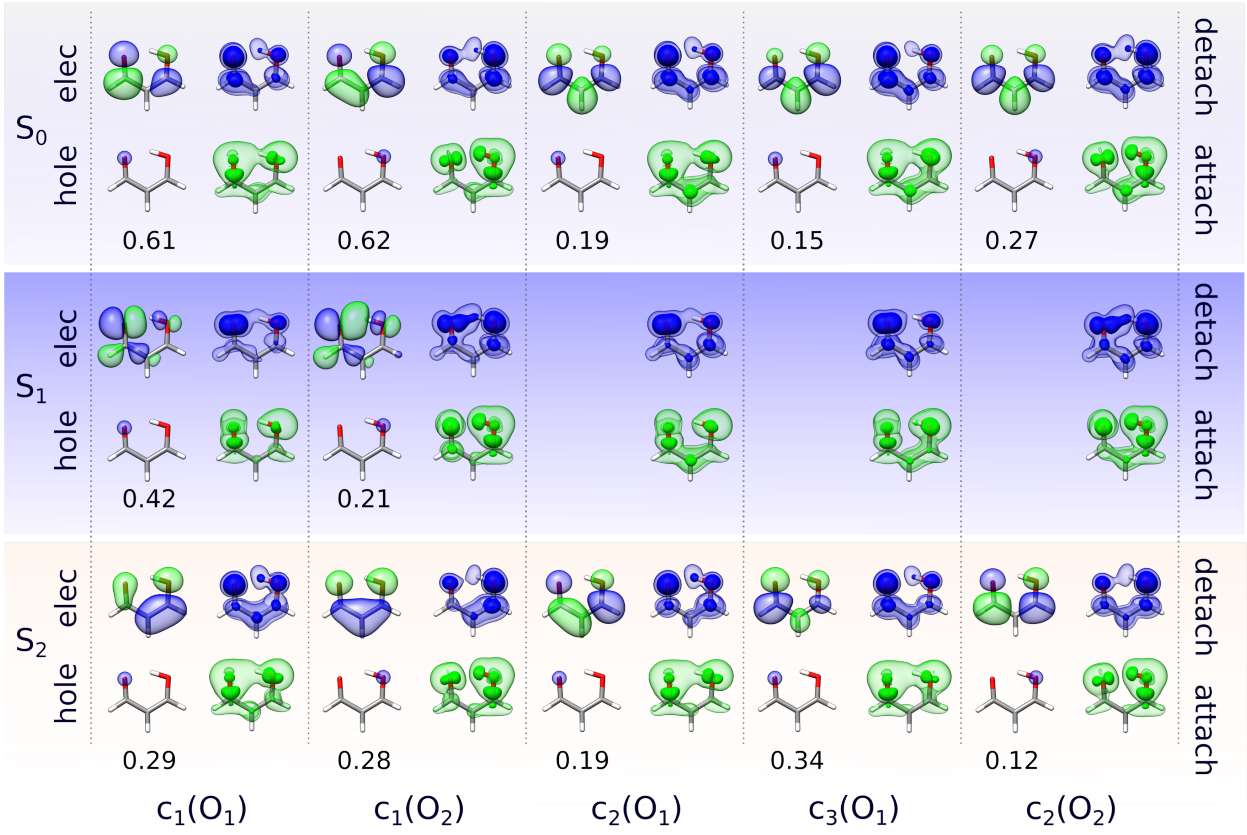

Figure S8 Comparison of one-electron transition and difference density pictures of the lowest valence-to-core transitions from the S_0, S_1 and S_2 states at the FC point, as obtained at the RASPT2(18,0/1,0;2,12,0)/cc-pVDZ level of theory. For each core excitation, the dominant NTO pair (associated weight is listed below each pair) is shown on the left, and the detachment(green)/attachment(blue) densities on the right. A single NTO pair dominates each transition with the exception of the transitions from S_1 to $c_2(O_{1/2})$ and $c_3(O_1)$ that display negligible one-electron excitation character. Isosurface value for the NTO pairs: 0.03 a.u. Isosurface values for the densities: 0.02 a.u. (opaque), 0.004 a.u. (colored transparent).

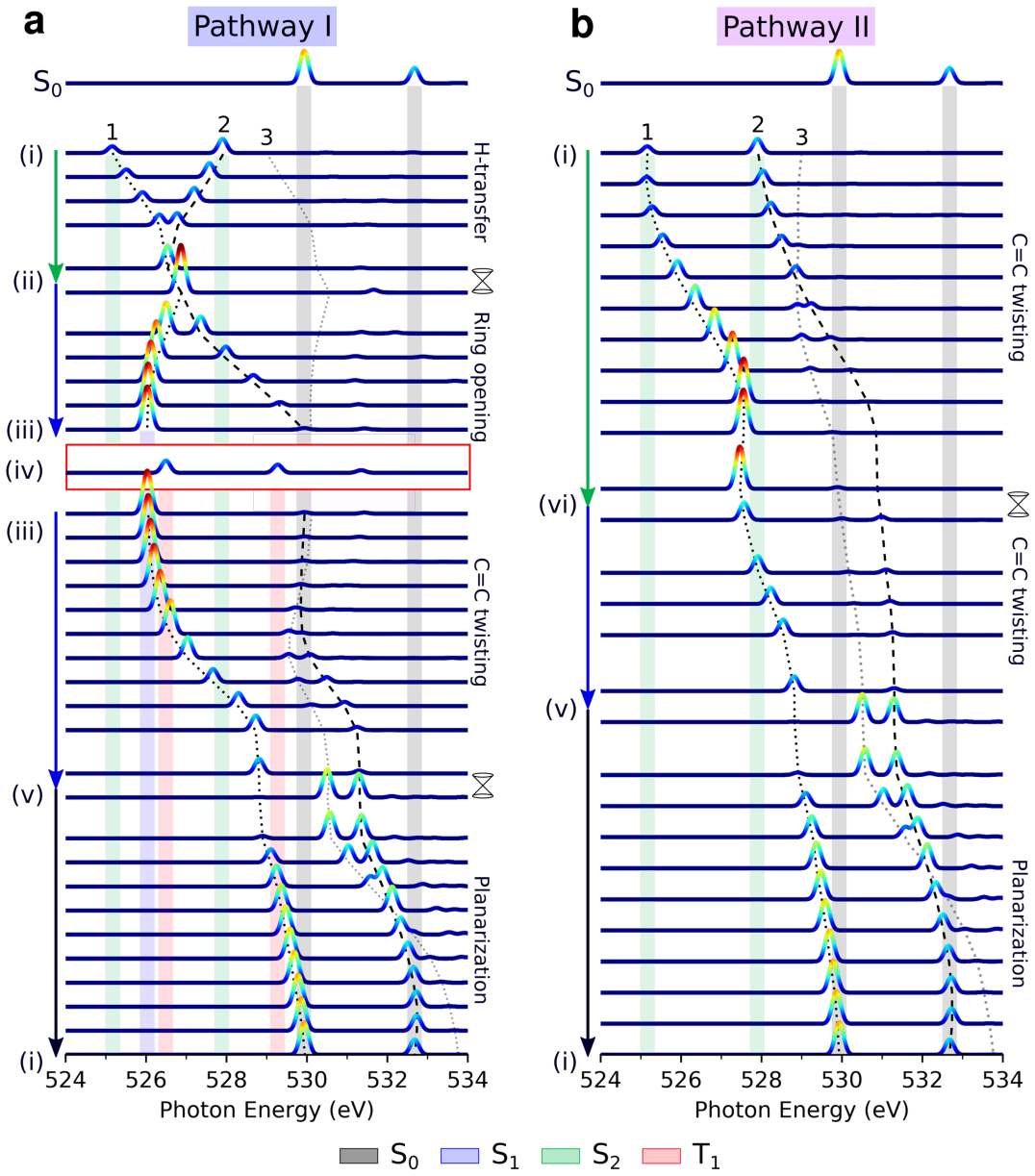

Figure S9 Same as in Figure 5 of the main text but with NEXAFS spectra computed at the CVS-ADC(2)-x/6-311++G** level of theory. Stick spectra were convolved with a Gaussian line shape (FWHM: 0.25 eV).

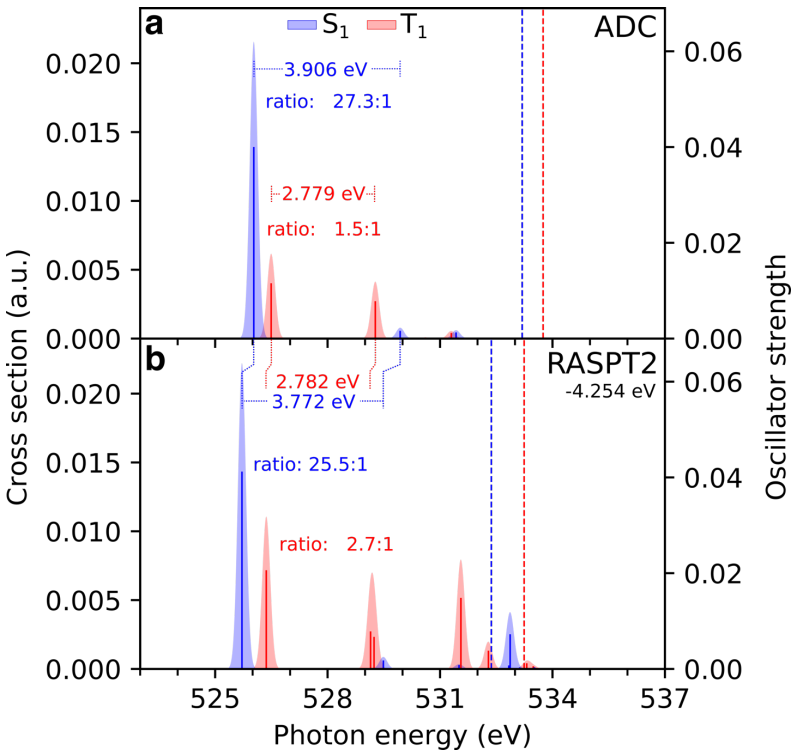

Figure S10 Comparison of oxygen *K*-edge NEXAFS spectra at the RASPT2 and ADC levels of theory for the lowest valence-excited singlet and triplet state (S_1: blue, T_1: red) at their respective minima. (a) CVS-ADC(2)-x/6-311++G**, and (b) RASPT2(18,0/1,0;2,12,0)/cc-pVDZ. The latter have been uniformly shifted by -4.254 eV to align with the steady-state spectrum at the ADC level. The lowest vertical core-ionization energies, corresponding to a 1s(O_1) hole, are indicated by dashed lines. Stick spectra were convolved with a Gaussian line shape (FWHM: 0.25 eV).

Coordinates

Table S5 The SA3-XMS-CASPT2(14,12)/cc-pVDZ geometry of S_0 minimum. Coordinates in Ångström.

Atom	x	y	z
O1	0.297883008782	1.041747096178	0.574294615037
O2	-1.902886748121	0.747930177316	1.898030367318
C1	0.017348979444	-0.005120884021	-0.041149386147
C2	-1.185497221386	-0.780774563890	0.204458075458
C3	-2.070554173346	-0.346060952878	1.166354889151
H1	0.713193004413	-0.377025618927	-0.820711499087
H2	-1.386986160493	-1.691288495884	-0.360812887694
H3	-2.993372821785	-0.889628916065	1.394861476963
H4	-1.032179614262	1.126383228879	1.577951601036

Table S6 The SA3-XMS-CASPT2(14,12)/cc-pVDZ geometry of S_1 minimum. Coordinates in Ångström.

Atom	x	y	z
O1	0.377034741919	1.120799408015	0.579890597738
O2	-2.067171910728	0.678419958000	1.959649835706
C1	0.063104508894	-0.012280994287	-0.078978062613
C2	-1.107041830453	-0.737049895463	0.183369947448
C3	-2.083492147997	-0.404458787523	1.129875019284
H1	0.805436036690	-0.308895288723	-0.831506405825
H2	-1.260150173409	-1.640410170880	-0.410019751813
H3	-2.971383004626	-1.020017638061	1.276795697165
H4	-1.259818699989	1.192426240858	1.790675578456

Table S7 The SA3-XMS-CASPT2(14,12)/cc-pVDZ geometry of T_1 minimum. Coordinates in Ångström.

Atom	x	y	z
O1	-0.579787894884	-0.623773472806	-0.365285126682
O2	0.698623967957	1.366342903219	0.878883124382
C1	-1.657789538692	-0.231826642822	0.199929307682
C2	-1.704226208925	0.948613622310	0.976841160389
C3	-0.533928641828	1.835960266046	1.176141608331
H1	-2.586809738896	-0.812626354292	0.069190541874
H2	-2.655018657227	1.245603159445	1.429980918945
H3	-0.556653021277	2.639821514497	1.912601624155
H4	0.535686187399	0.572333494320	0.307426523541

Table S8 The SA3-XMS-CASPT2(14,12)/cc-pVDZ geometry of hydrogen-transfer S_2/S_1 minimum energy conical intersection. Coordinates in Ångström.

Atom	x	y	z
O1	-1.196659105129	2.111558250455	0.000000690077
O2	1.200441778961	2.106602653835	0.000000015236
C1	-1.236696594263	0.786446715556	0.000000000000
C2	-0.002377868787	0.042671034588	0.000000000000
C3	1.235016448069	0.781331244466	-0.000000811566
H1	-2.222305057634	0.306891447566	0.000000599200
H2	-0.004642811776	-1.048182811635	-0.000001044591
H3	2.218642281326	0.297722731659	-0.000000741186
H4	0.002392250267	2.314007455056	0.000000413464

Table S9 The SA3-XMS-CASPT2(14,12)/cc-pVDZ geometry of twisted S_1/S_0 minimum energy conical intersection. Coordinates in Ångström.

Atom	x	y	z
O1	1.790860815639	2.321319179941	-0.135454182991
O2	-0.752107864787	-0.074640665680	-1.110704624069
C1	2.262499411580	1.179931009088	-0.047270198493
C2	1.450779874300	-0.022535316802	0.013653445807
C3	-0.012565500566	0.031349072823	0.038858488186
H1	3.363552864584	1.019966665470	-0.020420251639
H2	1.983706259574	-0.987665730216	0.030911832534
H3	-0.612618572725	-0.075549176370	0.945367580537
H4	-0.144396889947	0.075381545083	-1.853789094707

Table S10 The SA3-XMS-CASPT2(14,12)/cc-pVDZ geometry of twisted S_2/S_1 minimum energy conical intersection. Coordinates in Ångström.

Atom	x	y	z
O1	1.967343296650	2.445542505971	-0.065297231759
O2	-0.790521628005	-0.306050086636	-1.105505717780
C1	2.227730397174	1.166466858892	-0.053448522917
C2	1.389958078105	0.073572896139	-0.024796729469
C3	-0.071991768844	0.112580862638	-0.007609456868
H1	3.323341998566	1.011060171382	-0.038560166484
H2	1.925764675023	-0.885305428738	0.023292928905
H3	-0.671938490458	0.112311742491	0.905864963112
H4	-0.161371795998	-0.331699574159	-1.844795866325

References

1. J. Schirmer, *Phys. Rev. A*, 1982, **26**, 2395.
2. J. Schirmer, *Phys. Rev. A*, 1991, **43**, 4647.
3. J. Schirmer and A. Trofimov, *J. Chem. Phys.*, 2004, **120**, 11449-11464.
4. M. Wormit, D. R. Rehn, P. H. Harbach, J. Wenzel, C. M. Krauter, E. Epifanovsky and A. Dreuw, *Mol. Phys.*, 2014, **112**, 774-784.
5. L. S. Cederbaum, W. Domcke and J. Schirmer, *Phys. Rev. A*, 1980, **22**, 206.
6. A. Barth and J. Schirmer, *J. Phys. B: At. Mol. Phys.*, 1985, **18**, 867.
7. A. Barth and L. Cederbaum, *Phys. Rev. A*, 1981, **23**, 1038.
8. A. Dreuw and M. Wormit, *Wiley Interdiscip. Rev. Comput. Mol. Sci.*, 2015, **5**, 82-95.
9. J. Wenzel, M. Wormit and A. Dreuw, *J. Comput. Chem.*, 2014, **35**, 1900-1915.
10. J. Schirmer and F. Mertins, *Int. J. Quantum Chem*, 1996, **58**, 329-339.
11. D. R. Rehn, A. Dreuw and P. Norman, *J. Chem. Theory Comput.*, 2017, **13**, 5552-5559.
12. M. Head-Gordon, *Chem. Phys. Lett.*, 2003, **372**, 508-511.
13. M. Sapunar, T. Ayari and N. Došlić, *Chem. Phys.*, 2018, **515**, 622-627.
14. F. Plasser, M. Wormit and A. Dreuw, *J. Chem. Phys.*, 2014, **141**, 024106.